mater.scichina.com link.springer.com https://doi.org/10.1007/s40843-025-3883-2

Stress-induced anisotropy for MHz-stable permeability in Fe-based nanocrystalline alloys

Zhijun Guo[†], Jifeng Zhou[†], Qianqian Liu, Mingjuan Cai, Yanzhou Fan, Qiang Luo[*] and Baolong Shen[*]

ABSTRACT **Tensile stress annealing (TSA) is an effective strategy for tailoring magnetic anisotropy and high-frequency performance in nanocrystalline soft magnetic alloys. Here, we systematically investigate the influence of TSA on the microstructure, magnetic domain evolution, and permeability stability of $Fe_{69.5}Co_3Nb_2Mo_{1.5}Si_{14}B_9Cu_1$ nanocrystalline alloys. Across all applied stresses (0–300 MPa), the alloys retain an ultrafine grain size (⩽11 nm), yet the induced uniaxial anisotropy constant (K_u) rises sharply from 22.5 to 665 J/m^3. This increase in K_u refines the magnetic domain structure, reducing average domain width from 110 to 36 μm, and shifts the magnetization mechanism from domain-wall displacement to rotation-dominated reversal. Quantitative correlation between K_u, domain structure, and effective permeability (μ_e) reveals that higher stress suppresses μ_e at low frequencies but yields exceptional frequency stability: $\mu_e \approx 2330$ is maintained up to 1 MHz at 50 MPa, and $\mu_e \approx 585$ remains constant from 1 kHz to 10 MHz at 300 MPa. These findings demonstrate that stress-induced anisotropy is a decisive factor in governing high-frequency magnetic response, offering both mechanistic insight and a practical framework for designing next-generation soft magnetic materials for precision current transformers, EMC filters, and MHz-class power electronics.**

Keywords: tensile stress annealing, magnetic anisotropy, domain structure evolution, high-frequency permeability stability, Fe-based nanocrystalline alloy

INTRODUCTION

The rapid evolution of power electronics has intensified the demand for magnetic components capable of operating efficiently at high frequencies, often in the MHz range. Devices such as current transformers, DC-DC power converters, and electromagnetic compatibility (EMC) filters are integral to smart grids, electric vehicles, renewable energy systems, and high-speed communication infrastructure [1–3]. However, the proliferation of rectifiers, inverters, and high-frequency switching circuits introduces substantial DC and harmonic components into the power grid. These effects induce nonlinear magnetic behavior and permeability degradation in transformer cores, ultimately compromising measurement accuracy and efficiency. Achieving low, stable effective permeability (μ_e) under high-frequency excitation and DC-bias is therefore critical for suppressing electromagnetic interference and ensuring reliable performance in next-generation power systems [4,5].

Fe-based nanocrystalline alloys are a prime candidate for such applications due to their unique amorphous-nanocrystalline dual-phase structure, which combines high saturation magnetic flux density (B_s), high μ_e, low coercivity (H_c), and low core loss (P_{cv}) [6–8]. Yet under DC-bias, these alloys are prone to saturation, where μ_e declines sharply even at relatively low DC-bias fields, severely restricting their usable frequency range. Conventional strategies, such as Ni alloying [9] or magnetic field annealing [10], are commonly employed to modulate K_u to mitigate this effect. However, their effectiveness is often limited by intrinsic trade-offs. While Ni alloying can tune μ_e to a certain degree, it adversely affects frequency stability. Additionally, magnetic field annealing results in mediocre permeability linearity and inadequate DC-bias tolerance.

Among Fe-based nanocrystalline systems, the FINEMET-type alloys are particularly attractive for high-frequency applications due to their excellent amorphous-forming ability and well-defined nanocrystalline structure, favorable μ_e and P_{cv} [11–13]. Thus, it is a promising candidate for developing high-frequency soft magnetic materials. However, further optimization of alloy composition and annealing processes is critical to enhance its high-frequency performance. Notably, adjusting the Co content has been demonstrated as an effective approach to improving both soft magnetic properties and thermal stability. The incorporation of Co enhances both B_s and Curie temperature (T_c), while simultaneously contributing to the refinement and stabilization of the nanocrystalline structure, suppressing grain growth and thereby maintaining optimal soft magnetic properties [14–16]. However, the effect is intrinsically dualistic. While Fe–Co strong exchange coupling contributes to improved thermal stability, reduced H_c, and elevated μ_e [15,17,18], excessive Co content can disrupt microstructural homogeneity due to its high magnetocrystalline anisotropy energy, leading to increased K_u and deteriorated soft magnetic properties [19–23]. Striking the right compositional balance is therefore essential before applying post-processing treatment. Nb and Mo are utilized to improve glass-forming ability, suppress grain growth, and stabilize the nanocrystalline structure during annealing [24,25]. Tensile stress annealing (TSA) offers a far more powerful route to K_u control than magnetic field annealing, typically achieving two orders of magnitude greater anisotropy modulation [26]. TSA can produce Fe-based nanocrystalline alloys with precisely tuned μ_e and exceptional frequency stability [26–28]. In a preceding study, Cai *et al.* reported on optimizing soft magnetic

School of Materials Science and Engineering, Jiangsu Key Laboratory for Advanced Metallic Materials, Southeast University, Nanjing 211189, China
† Equally contributed to this work.
* Corresponding author (email: q.luo@seu.edu.cn; blshen@seu.edu.cn)

properties in FeCoSiBPC amorphous alloys characterized by a high B_s [29]. Through the TSA, a marked improvement in μ_e and a decrease in magnetic loss were realized. Cai *et al.* successfully prepared $Fe_{74-x}Co_xSi_{13}B_8Nb_2Cu_1Mn_2$ (x = 0, 2, 4, 6, 8) nanocrystalline alloys via static TSA, achieving high-frequency μ_e stability and strong DC bias resistance [30]. However, the frequency range of permeability stability of this work is not wide enough and can only be maintained within 1 MHz. Furthermore, Guo *et al.* [31] reported the fabrication of a $Fe_{73.5}Si_{15.5}B_7Nb_3Cu_1$ nanocrystalline alloy treated by TSA. This alloy exhibited excellent frequency stability with a constant μ_e of 400 over a wide operational range from 1 kHz to 10 MHz. However, the value of 400 in μ_e is insufficient for applications requiring higher inductance.

In this work, $Fe_{72.5-x}Co_xNb_2Mo_{1.5}Si_{14}B_9Cu_1$ (x = 1, 3, 5, 7) was deliberately designed based on careful considerations of structural stability and soft magnetic optimization. After systematic compositional selection, $Fe_{69.5}Co_3Nb_2Mo_{1.5}Si_{14}B_9Cu_1$ alloy exhibited the optimal combination of high B_s, low H_c, and stable μ_e. It was thus selected for subsequent TSA investigation. To improve the frequency stability and magnitude of effective permeability at high frequencies. We systematically examine the effects of varying Co element concentration and applying TSA on the soft magnetic characteristics of the $Fe_{69.5}Co_3Nb_2Mo_{1.5}Si_{14}B_9Cu_1$ nanocrystalline alloy. The crystallization behavior, K_u evolution, domain structure modulation with tensile stress level, and quantitatively linking these to frequency-dependent μ_e with core loss were systematically correlated. Benchmarking against other Fe-based nanocrystalline alloys confirms that the present approach achieves an unprecedented combination of permeability stability, hysteresis linearity, and high-frequency resilience. These findings provide both mechanistic insight and practical design principles for next-generation soft magnetic materials for high-frequency power electronics, including precision current transformers, EMC filters, MHz-class switching devices for electric vehicles, and 5G communication systems.

EXPERIMENTAL SECTION

Alloy ingots with compositions of $Fe_{72.5-x}Co_xNb_2Mo_{1.5}Si_{14}B_9Cu_1$ (x = 1, 3, 5, 7) were prepared by induction melting the mixtures of Fe (99.99 wt.%), Co (99.99 wt.%), Nb (99.999 wt.%), Mo (99.999 wt.%), Si (99.999 wt.%), B (99.99 wt.%), and Cu (99.999 wt.%) under an argon atmosphere. The as-quenched (AQ) ribbons were fabricated by single-roller melt spinning, and the thickness was 20 ± 2 μm. The thermal properties were analyzed by a differential scanning calorimeter (DSC, Netzsch 404 F3). TSA treatments were performed at 818 K for 10 min under applied tensile stresses of 0–300 MPa, followed by rapid forced-air cooling. This annealing temperature (818 K) was chosen because preliminary DSC measurements and isothermal trials identified it as optimal for controlled nanocrystallization of the Fe-Co-Nb-Mo-Si-Cu ribbons. The initial magnetization curves and hysteresis loops were measured by the vibrating sample magnetometer (VSM, Lake Shore 7407), and the B_s was determined under an applied field of 800 kA/m. The μ_e, H_c and P_{cv} were measured by an impedance analyzer (Keysight, E4990A), a DC B-H loop tracer (Riken, BHS-40) under a maximum field of 1 kA/m and an AC B-H loop tracer (Riken, AC BH-100), respectively. The microstructure was characterized by X-ray diffraction (XRD, Bruker D8-Discover) with Cu K_α radiation, and transmission electron microscopy (TEM, Talos F200X). The average grain size of nanocrystals (D_{av}) was estimated from the grain size distribution of nanocrystals in selected bright field TEM images using *Nano Measurer* software and Gaussian fitting. The magnetic domain was analyzed employing a magneto-optical Kerr microscope (Evico Magnetics GmbH, em-Kerr-highres).

RESULTS AND DISCUSSION

The XRD pattern of AQ $Fe_{72.5-x}Co_xNb_2Mo_{1.5}Si_{14}B_9Cu_1$ (x = 1, 3, 5, 7) ribbons reveals a typical broad diffuse halo, with no discernible sharp diffraction peaks (Fig. 1a), confirming the formation of a fully amorphous structure. The DSC analysis demonstrates a distinct two-stage crystallization process, corresponding to the sequential precipitation of α-Fe(Co) and Fe-metalloid compounds (Fig. 1b). As the Co content increases, the initial crystallization temperature (T_{x1}) rises from 815 to 819 K, while the secondary crystallization temperature (T_{x2}) remains relatively unchanged, indicating that the addition of Co marginally enhances the thermal stability of the alloys. Moreover, the alloys exhibit a broad crystallization temperature interval ΔT ($\Delta T = T_{x2} - T_{x1}$) ranging from 149 to 152 K, which is a critical parameter for evaluating thermal stability and guiding nanocrystallization kinetics. A larger ΔT promotes uniform nucleation and growth of fine α-Fe(Co) grains while effectively suppressing the formation of undesirable secondary phases,

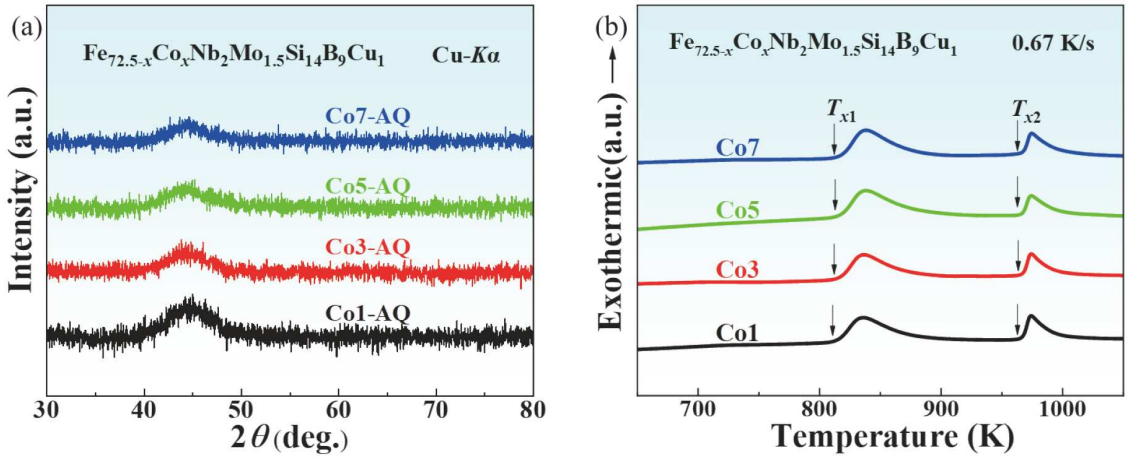

Figure 1 (a) XRD patterns, (b) DSC curves of AQ $Fe_{72.5-x}Co_xNb_2Mo_{1.5}Si_{14}B_9Cu_1$ (x=1, 3, 5, 7).

thereby preserving optimal soft magnetic properties.

All Co1–Co7 alloys demonstrated optimal soft magnetic properties when annealed at 818 K. To quantitatively assess their soft magnetic behavior under these conditions, the μ_e (1 A/m, measured at 1, 10, and 100 kHz), H_c, and B_s were analyzed for each alloy composition with different annealing durations (10, 30 and 60 min), as illustrated in Fig. 2a–c. As shown in Fig. 2a, the μ_e value for all compositions decreases with increasing test frequency. At 10 min of annealing, μ_e ranges from 43800 to 46700 at 1 kHz, 39200 to 40900 at 10 kHz, and 19000 to 19200 at 100 kHz. Extending the annealing duration to 30 min enhances μ_e across all frequencies, reaching 47990–50900 (1 kHz), 40870–41530 (10 kHz), and 19060–19910 (100 kHz). Further extension to 60 min results in a continued increase in μ_e, peaking at 48700–51260 (1 kHz), 43300–47250 (10 kHz), and 21090–21650 (100 kHz). These trends indicate that prolonged annealing improved domain wall mobility and reduced magnetoelastic energy, particularly at higher frequencies where μ_e stability is critical. Fig. 2b shows that the H_c exhibits a slight but consistent increase with prolonged annealing, which is inversely correlated with the observed enhancement in μ_e. According to Herzer's classical stochastic anisotropy model, this behavior can be attributed to the interplay between grain refinement and magnetic domain wall dynamics. Theoretically, H_c scales inversely with magnetic polarization strength (J_s), while μ_e is proportional to J_s^2 [32]. Thus, an increase in J_s due to improved microstructural ordering has a stronger impact on μ_e than on H_c. Fig. 2c shows that B_s also increase steadily with annealing time, which reflects enhanced magnetic polarization and a more uniform nanocrystalline structure. The simultaneous increase in μ_e and B_s, despite a modest rise in H_c, underscores the critical role of optimized annealing in tuning the magnetic softness and frequency stability of the alloys. Among all tested compositions, Co3 alloy emerges as the most promising candidate, exhibiting the lowest H_c, the highest μ_e, and relatively high B_s, all achieved with a moderate Co content. These attributes balance magnetic performance with compositional economy. Consequently, the Co3 alloy was selected for subsequent TSA to further tailor its K_u and high-frequency behavior (Figs S1 and S2).

To clarify the influence of σ on the soft magnetic properties of Co3 alloys, TSA was conducted at an optimized temperature (818 K) for 10 min. The frequency-dependence μ_e of the annealed ribbons under various tensile stresses is presented in Fig. 3a. Increasing σ markedly enhances permeability stability across the tested frequency range. At 50 MPa, the alloys exhibit a high μ_e value that remains nearly constant from 1 kHz to 1 MHz. However, as σ increases from 50 to 100 MPa, the μ_e at 1 kHz decreases sharply from 2330 to 1640, while its frequency dependence becomes notably flatter, indicating improved stability up to 2 MHz. With further increases in σ, μ_e continues to decline at lower frequencies, yet maintains high frequencies. At 300 MPa, the alloy exhibits stable μ_e (~585) from 1 kHz to nearly 10 MHz, demonstrating excellent constant μ_e characteristics. This μ_e suppression at low frequencies, combined with enhanced frequency stability, arises from stress-induced K_u generated during annealing [33,34]. During nanocrystallization, the nanocrystals and amorphous phases exhibit different elastic moduli. The confinement of the amorphous phase causes partial

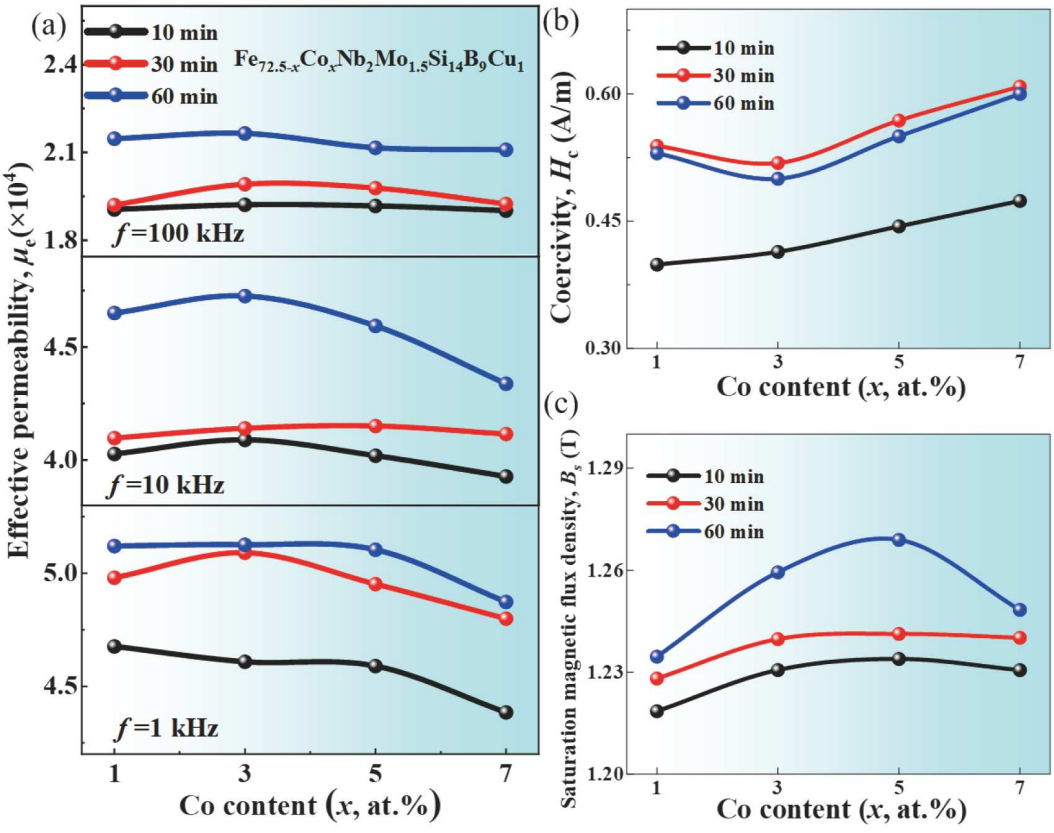

Figure 2 variation of (a) μ_e (measured at 1, 10, and 100 kHz), (b) H_c, and (c) B_s as a function of Co content for samples in stress-free conditions with annealing durations of 10, 30 and 60 min.

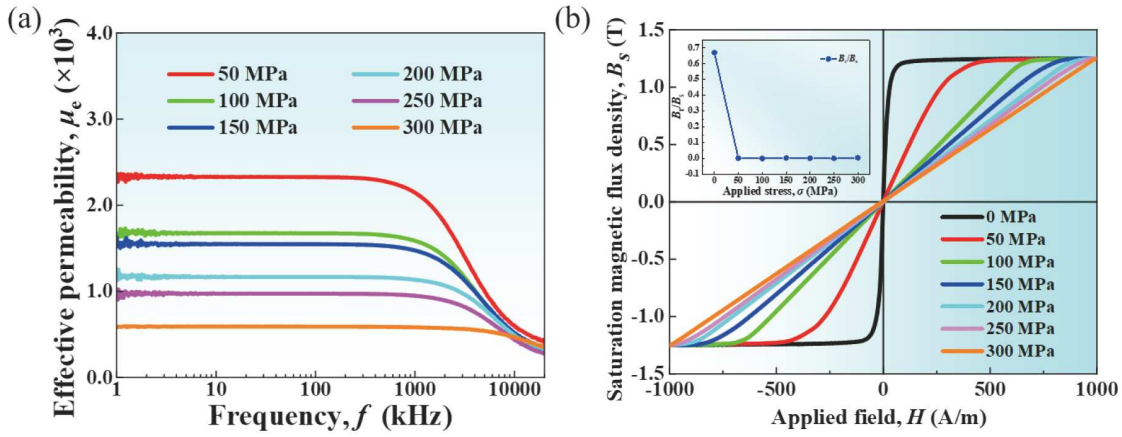

Figure 3 Frequency dependence of (a) μ_e and (b) static hysteresis loops of $Fe_{69.5}Co_3Nb_2Mo_{1.5}Si_{14}B_9Cu_1$ nanocrystalline alloy under various applied tensile stresses, the inset shows the variation of the remanence ratio (B_r/B_s) as a function of applied tensile stresses.

retention of elastic strain in the nanocrystalline phase after annealing, producing magnetoelastic anisotropy [35]. This results in a stable hard magnetization axis parallel to the applied stress, reducing μ_e while stabilizing its frequency response. Excessive σ may cause ribbons to fracture, thereby imposing a practical limit on stress-enhanced K_u and constant μ_e tuning, which can provide guidance for industrial-scale production. The influence of σ is further reflected in static hysteresis loops (Fig. 3b). Compared with the 0 MPa state, the hysteresis loops under tensile stress are progressively flatter, consistent with the development of a hard magnetization axis. The hysteresis loops consist of a linear region with nearly constant μ_e and a nonlinear saturation region. Such a wide linear range is particularly advantageous for a current transformer, where minimal permeability variation under DC-bias reduces measurement errors [36]. As shown in the inset of Fig. 3b, the remanence ratio (B_r/B_s) was extracted from the static hysteresis loops to quantify the evolution of magnetization behavior under tensile stress. The B_r/B_s values decrease monotonically from ~0.68 at 0 MPa to 0.005 at 300 MPa, indicating a gradual transition of the magnetization mechanism from domain-wall displacement to rotation-dominated reversal [37]. The near-zero B_r/B_s at 300 MPa confirm that the applied stress induces a strong uniaxial anisotropy, which constrains domain-wall motion and enforces coherent rotation during magnetization.

While σ offers clear benefits for frequency stability, Fig. 4a, b illustrates the variation of H_c and P_{cv} in $Fe_{69.5}Co_3Nb_2Mo_{1.5}Si_{14}B_9Cu_1$ nanocrystalline alloy ribbons as a function of σ. Both H_c and P_{cv} values exhibit an increasing trend with rising σ. This behavior is primarily attributed to lattice distortion in the nanocrystalline phases, which is induced by external mechanical σ and results in enhanced magnetocrystalline anisotropy [34]. In addition, magnetoelastic anisotropy arises from the elastic interactions between the nanocrystals and the surrounding amorphous matrix, which is a consequence of their differing elastic moduli [35]. This anisotropy acts as an energy barrier to magnetic domain wall motion, thereby contributing to an increase in H_c [36]. Consequently, the heightened resistance to domain wall propagation leads to elevated P_{cv}. Although domain refinement is generally beneficial for reducing high-frequency loss, the markedly higher P_{cv} observed at 300 MPa can be attributed to the excessive stress-induced anisotropy. Under such high tensile stress, the K_u increases to approximately 665 J/m^3, which strongly constrains domain-wall displacement and shifts the magnetization mechanism toward coherent rotation. This rotation-dominated reversal requires higher magnetization energy, thereby increasing both hysteresis and eddy-current losses. Furthermore, the high elastic strain accumulated within the α-Fe(Co) nanocrystals introduces additional magnetoelastic damping [38,39], which contributes to the overall rise in P_{cv}. Hence, despite finer domain structures, the enhanced anisotropy and magnetoelastic effects under 300 MPa collectively lead to a higher total core loss. Therefore, when the applied tensile stress is high, the H_c and P_{cv} of the nanocrystalline alloy are elevated due to the increased secondary-introduced internal stresses and stress-induced anisotropy [38].

To verify and quantify K_u, transverse initial magnetization curves were measured and demagnetization-corrected for samples annealed at 818 K for 10 min under tensile stresses of 0 (stress-free), 50, 100, 200, and 300 MPa (Fig. 4c, d). The anisotropy field (H_k) is defined as the magnetic field at which the tangent to the steepest slope of the initial magnetization curve and the B_s, obtained by extrapolating the tangent to H=0 [40]. TSA markedly increases H_k, from 36 A/m in the stress-free sample to 325 A/m at 50 MPa and up to 1065 A/m at 300 MPa, significantly exceeding the respective H_c. K_u can be calculated using:

$$K_u = \frac{H_k B_s}{2}. \quad (1)$$

Graphically, this corresponds to the shaded triangle area (pink) in Fig. 4c, d. K_u increases from 22.5 J/m^3 in the stress-free state to 203 J/m^3 at 50 MPa to 665 J/m^3 at 300 MPa. The relatively low K_u at 50 MPa explains the persistence of mobile domain walls and the less uniform domain configuration observed during magnetization. This clearly indicates that the average anisotropy is predominantly dominated by stress-induced K_u. The dependence of K_u on σ is consistent with prior reports [33,38] and expressed as follows [27,41]:

$$K_u = \frac{3}{2}\lambda_s^{FeSi}\sigma x_{cr} = \frac{B_s^2}{2\mu_0\mu_e}. \quad (2)$$

Here, λ_s^{FeSi} is the saturation magnetostriction coefficient of the α-Fe(Si) phase, σ is the applied σ, x_{cr} denotes the crystal volume fraction, and μ_0 is the vacuum permeability. According to this

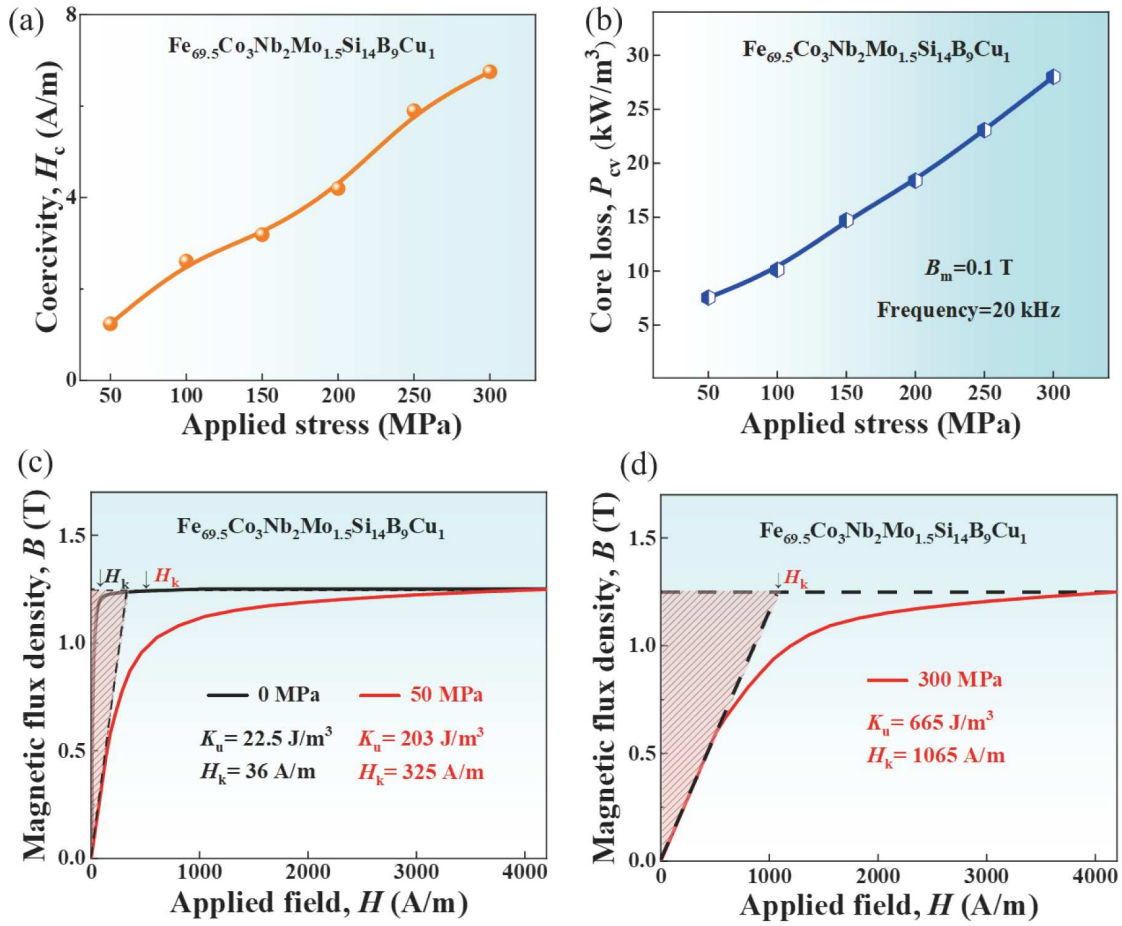

Figure 4 (a) H_c and (b) P_{cv} curves of $Fe_{69.5}Co_3Nb_2Mo_{1.5}Si_{14}B_9Cu_1$ nanocrystalline alloy under various tensile stresses; Initial magnetization curves measured transversally and corrected for the demagnetization effect of $Fe_{69.5}Co_3Nb_2Mo_{1.5}Si_{14}B_9Cu_1$ nanocrystalline samples annealed by TSA: (c) 0 and 50 MPa, (d) 300 MPa.

relationship, the reduction in μ_e with increasing σ arises from the increase in K_u, which suppresses the domain wall mobility and enhances permeability stability through anisotropy control. A quantitative comparison between the experimentally derived and theoretically estimated K_u values was conducted to further confirm the validity of the stress anisotropy relationship. The theoretical K_u was calculated according to Eq. (2). For σ = 50–300 MPa, the theoretical K_u ranges from 226 to 621 J/m^3 (Table S1), which is well matched with the experimental K_u values (203–665 J/m^3) obtained from Fig. 4d. This consistency confirms that the observed anisotropy enhancement originates predominantly from the magnetoelastic effect induced by tensile stress.

While increasing the σ moderately elevates H_c and P_{cv}, it markedly suppresses the rapid decline of μ_e with frequency, an essential characteristic for maintaining stable magnetic performance in high-frequency regimes. Fig. 5 benchmarks the frequency and μ_e of $Fe_{69.5}Co_3Nb_2Mo_{1.5}Si_{14}B_9Cu_1$ nanocrystalline alloy against other representative Fe-based nanocrystalline alloys [30,36,38,40,42–52]. The results clearly position the present alloy in a unique performance window, which combines constant μ_e characteristics with a substantially extended frequency that is well beyond most conventional nanocrystalline compositions. These advantages directly reflect the efficacy of TSA in tailoring K_u and domain dynamics. By balancing stress-induced anisotropy with microstructural optimization, the present approach achieves a rare combination of μ_e stability, high-frequency resilience, and application-relevant loss characteristics. Consequently, the $Fe_{69.5}Co_3Nb_2Mo_{1.5}Si_{14}B_9Cu_1$ alloy emerges as a promising candidate for advanced magnetic components in high-frequency power electronics, including current transformers, high-speed inductors, and EMC filters.

Co3 alloy was conducted by XRD analysis, and stress-free annealing was set as the control to elucidate whether σ affects the microstructure of alloys. As shown in Fig. 6a, all samples exhibit distinct diffraction peaks at 2θ = 45.1°, 65.7°, and 83.3°, which correspond to the (110), (200), and (211) crystal planes of the α-Fe(Co) phase, respectively. Since all samples were annealed under identical thermal conditions, the intensities and positions of the crystalline diffraction peaks remain largely unchanged across the different σ states. Fig. 6b–d shows the TEM bright-field images, SAED patterns, and grain size distribution histograms for samples subjected to tensile stresses of 0, 50, and 300 MPa. The bright-field TEM images reveal a homogenous dispersion of nanocrystals embedded within the amorphous matrix. The corresponding SAED patterns display typical ring diffraction fringes, confirming the α-Fe(Co) phase, in agreement with the XRD results. The average grain sizes for samples annealed under 0, 50, and 300 MPa are 11, 11, and 10 nm, which remain essentially unchanged under different applied stresses.

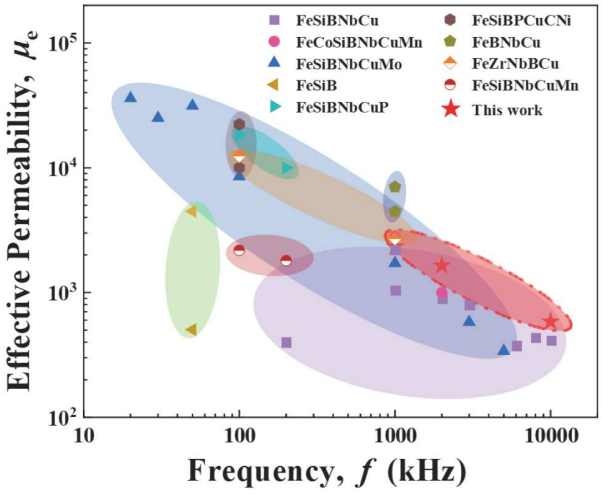

Figure 5 A summary of frequency and μ_e of the nanocrystalline alloys prepared in this work and other representative Fe-based nanocrystalline alloys.

This suggests that the variations in magnetic performance of TSA-treated samples mainly originate from K_u and dynamic domain structure evolution. Such structural stability is closely related to the role of Mo in the alloy system. As a refractory element with low diffusivity, Mo prefers to segregate between α-Fe(Co) and amorphous interfaces, which effectively suppresses grain coarsening and promotes nanocrystal dispersion during TSA. Therefore, the differences in magnetic properties induced by TSA can be primarily attributed to changes in K_u and domain structure, rather than variations in crystallization behavior.

The dynamic magnetic domain structure and magnetization process were systematically investigated to further elucidate how the magnitude of σ influences the soft magnetic properties. Fig. 7 illustrates dynamic magnetic domain evolution during magnetization of the samples subjected to TSA at 0, 50, and 300 MPa. At H = 0 kA/m (demagnetized state), the magnetic domains in the 0 MPa sample exhibit irregular morphologies characterized by curved domain walls and disordered distributions, attributable to the inhomogeneous magnetization effects caused by average random anisotropy [38]. In contrast, samples subjected to applied σ exhibit pronounced changes in domain configuration. Broad strip-like domains emerge, separated by 180° straight domain walls, indicating that the hard magnetization axis tends to be parallel to the direction of tensile stress (i.e., the direction of the ribbons), whereas the easy magnetization axis is perpendicular to the direction of the ribbons [53–55]. As the σ increases, the average magnetic domain width ($\overline{d}$) gradually decreases, while the domain wall density increases significantly. The $\overline{d}$ is typically modulated by K_u and the domain wall energy (ε_ω). The theoretical relationship between $\overline{d}$ and K_u can be expressed as [56]:

$$\overline{d}=\sqrt{\frac{2\varepsilon_\omega t}{K_u}}, \tag{3}$$

$$\varepsilon_\omega=b\sqrt{AK_u}, \tag{4}$$

where t, b, and A are the ribbon thickness, a constant, and the alloy exchange interaction coefficient, respectively. According to this relationship, $\overline{d}$ is proportional to $(K_u)^{-1/4}$ and $(\varepsilon_\omega)^{-1/2}$. From Eqs. (2–4), increasing σ enhances both K_u and ε_ω, leading to a reduction of $\overline{d}$. Experimentally, under 50 MPa, the domain structure displays a strip-like pattern, though the domain walls

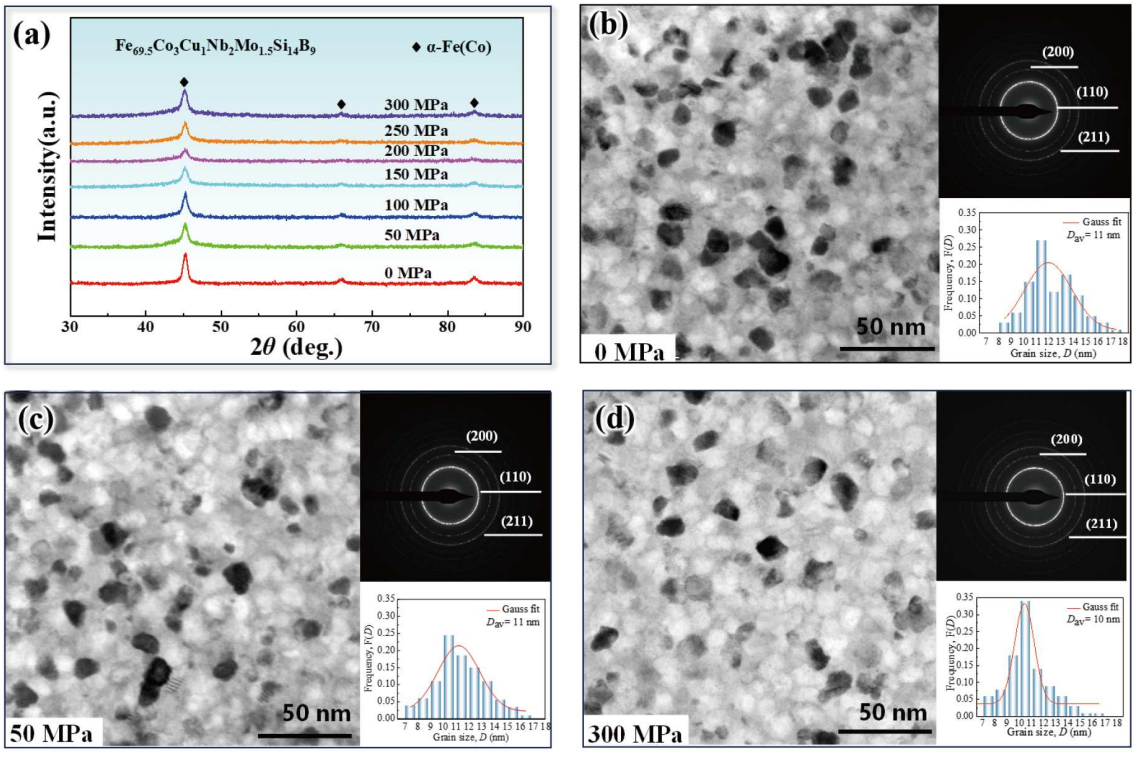

Figure 6 (a) XRD pattern of $Fe_{69.5}Co_3Nb_2Mo_{1.5}Si_{14}B_9Cu_1$ nanocrystalline ribbons annealed under various applied stresses. TEM images, SAED patterns, and grain size distributions of the $Fe_{69.5}Co_3Nb_2Mo_{1.5}Si_{14}B_9Cu_1$ nanocrystalline ribbons annealed under different applied stresses: (b) 0 MPa; (c) 50 MPa; (d) 300 MPa.

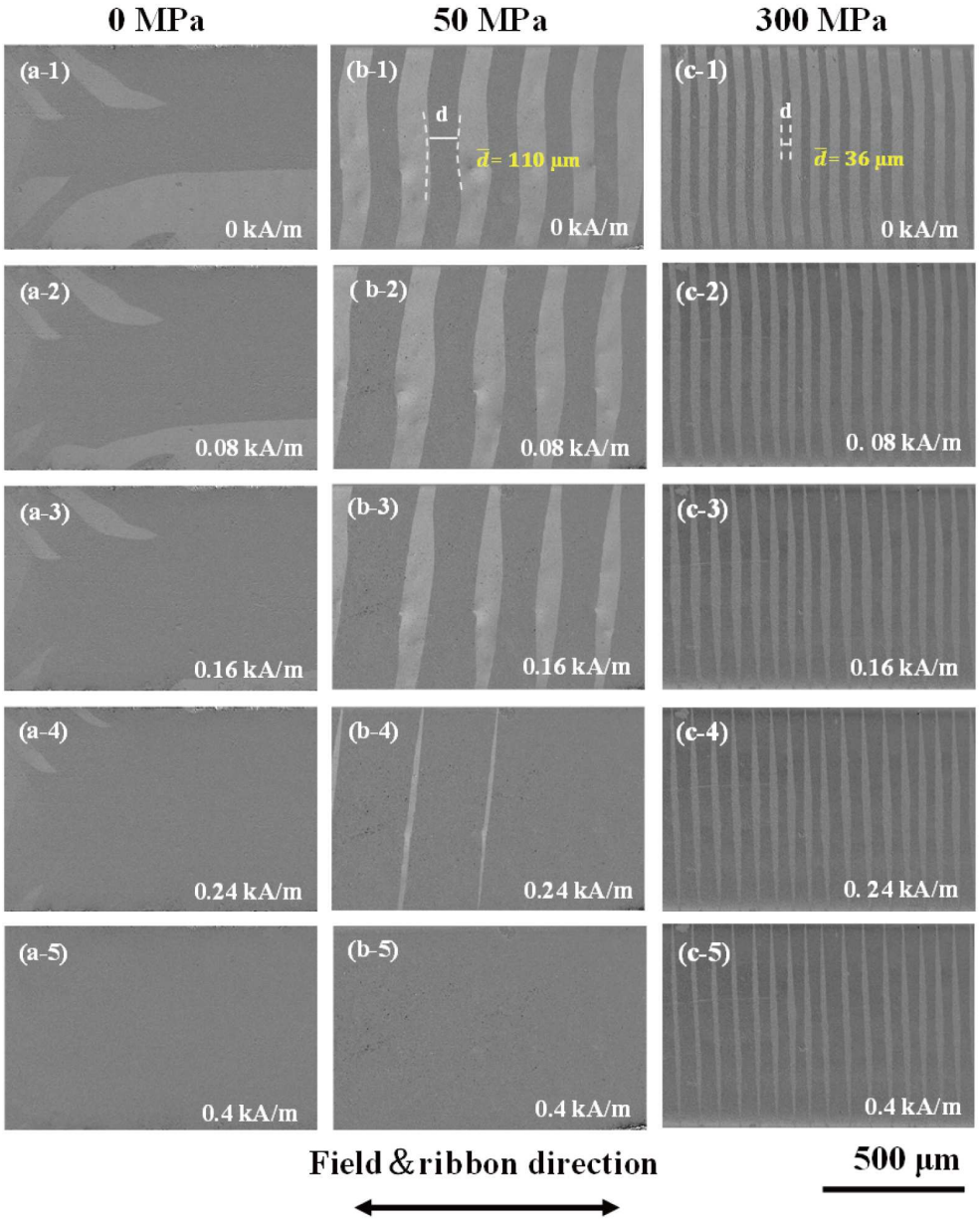

Figure 7 Dynamic magnetic domain evolution patterns of $Fe_{69.5}Co_3Nb_2Mo_{1.5}Si_{14}B_9Cu_1$ nanocrystalline ribbon samples annealed under different tension stresses: (a) 0 MPa, (b) 50 MPa, and (c) 300 MPa.

remain partially curved and unevenly spaced, with $\bar{d}$ value reaching a maximum of 110 μm. This suggests that the distribution of K_u within the ribbon samples is still heterogeneous and the induced stress anisotropy remains relatively weak. With further increase in σ to 300 MPa, the magnetic domain structure becomes more regularly aligned, and the $\bar{d}$ decreases sharply to approximately ~36 μm. The domain walls become more uniformly distributed, indicating the establishment of a strong and homogeneously distributed stress-induced K_u.

The magnetization process also varies with σ. In the 0 MPa sample, the magnetization process is primarily governed by domain wall displacement, accompanied by localized magnetization fluctuations on the micrometer scale. The saturation field occurs at 0.4 kA/m. At 50 MPa, wall displacement remains significant, but wall tilting emerges, indicating a transition to a mixed displacement–rotation mechanism [40]. At 300 MPa, the sample exhibits a fundamentally different dynamic response. Even under a 0.4 kA/m, the domain pattern remains largely unchanged, with clear evidence of magnetization rotation behavior dominating the reversal process. These results suggest that under large σ, the magnetization process is predominantly via coherent rotation, accompanied by minor domain wall displacement. According to Eqs. (3) and (4), both K_u and ε_ω increase with σ. The rise in K_u facilitates domain alignment and regularization, resulting in a lamellar domain structure with uniform distribution. Consequently, the energy required for domain wall movement becomes more consistent across the sample, contributing to homogeneous domain dynamics and a stabilized permeability response. Simultaneously, the increase in ε_ω elevates the energy barrier for domain rotation, restricting

magnetization changes and thereby reducing μ_e while improving the linearity of the hysteresis loops. This dual effect enhances the constant μ_e characteristics of the sample under high-frequency operating conditions. The variation in soft magnetic properties of $Fe_{69.5}Co_3Nb_2Mo_{1.5}Si_{14}B_9Cu_1$ nanocrystalline alloys subjected to TSA is intrinsically linked to changes in K_u.

Fig. 8 presents the relationships among K_u, $\overline{d}$, and μ_e for $Fe_{69.5}Co_3Nb_2Mo_{1.5}Si_{14}B_9Cu_1$ nanocrystalline alloys through annealing under varying σ. K_u increases monotonically with σ, reflecting the enhanced uniaxial strain retained in the distortion strain within the α-Fe(Co) phase during annealing. This strain originates from elastic mismatch between the amorphous and crystalline phases, inducing structural anisotropy (Δq) in the crystalline lattice of the α-Fe(Co) phase and thereby elevating both H_k and K_u [34,57]. Simultaneously, $\overline{d}$ decreases with increasing σ, governed by the coupled rise in ε_ω and K_u, as described in Eqs. (3) and (4). This narrowing of $\overline{d}$ reduces the spatial scale for magnetization rotation, lowering the energy differential for domain wall motion and enhancing frequency stability of the magnetic responses. The evolution in μ_e parallels the trend in $\overline{d}$: with higher K_u, magnetic exchange coupling between nanocrystals weakens [58], leading to a systematic decline in μ_e in accordance with Eq. (2). Moreover, the concurrent increase in ε_ω raises the energy barrier for magnetization reversal via domain wall rotation, further suppressing μ_e but improve both linearity and frequency stability, as previously demonstrated in Fig. 3a.

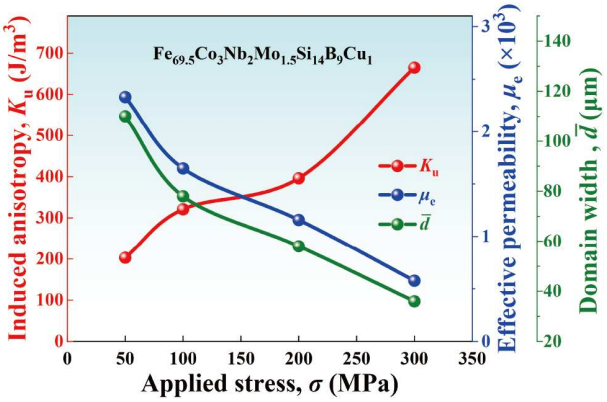

Figure 8 The dependence of K_u, $\overline{d}$, and μ_e of $Fe_{69.5}Co_3Nb_2Mo_{1.5}Si_{14}B_9Cu_1$ nanocrystalline alloys annealed by TSA with varying σ.

The schematic mechanism depicting the effect of σ on microstructure and domain evolution is shown in Fig. 9. In these diagrams, the pointers represent magnetic moments, the blue circles are nanocrystals, and the black double arrows indicate the average effective magnetic anisotropy <K> within the exchange correlation length (L_{ex}). In the as-quenched (AQ) state, the amorphous alloy displays a disordered magnetic domain configuration. After stress-free annealing (0 MPa TSA), nanocrystals

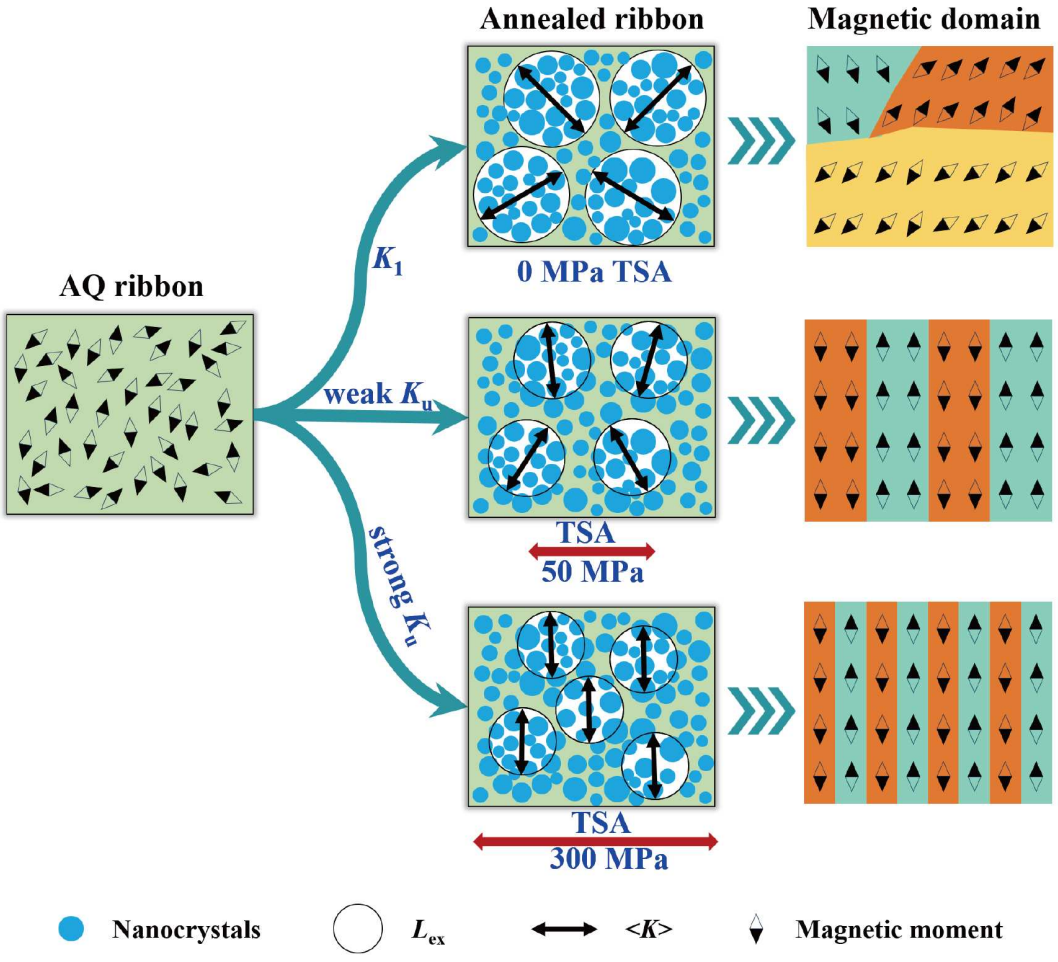

Figure 9 Schematic illustration of the effect of tensile stress on the induced anisotropy and magnetic domain structure.

form uniformly within the amorphous matrix, but the magnetization direction remains mostly random, with magnetocrystalline anisotropy (K_1) dominating, so the magnetic domain structure remains irregular. Conversely, TSA can induce a uniaxial anisotropy K_u, which is much larger than the K_1. At this point, the induced anisotropy becomes dominant in the alloy. As the stress increases, the magnetization gradually aligns perpendicular to the stress direction, with magnetic moments preferentially oriented away from the applied stress. Consequently, the magnetic domain structure evolves into a clear striped pattern with straight 180° domain walls, directly linked to the enhanced high-frequency soft magnetic performance observed in TSA-treated samples. Furthermore, based on the principle of minimum energy, the domain wall energy balances the magnetostatic energy and the anisotropy energy [59]. Therefore, as stress rises, the number of magnetic domain walls increases, resulting in finer magnetic domains.

CONCLUSIONS

TSA offers a powerful route to engineer magnetic anisotropy and domain structure in $Fe_{69.5}Co_3Nb_2Mo_{1.5}Si_{14}B_9Cu_1$ nanocrystalline alloys without compromising their ultrafine grain structure. Although the average grain size remains around 11 nm under all stress conditions, σ profoundly altered the K_u, which increases from 22.5 J/m^3 at 0 MPa to 665 J/m^3 at 300 MPa. The rise in K_u drives a systematic refinement of magnetic domains, reducing average domain width and transforming the magnetization process from domain-wall displacement to rotation-dominated reversal. By modulating K_u and domain structure, TSA enabled precise control over the μ_e and its frequency stability. Under moderate stress (50 MPa), $\mu_e \approx 2330$ is maintained up to 1 MHz, while at high stress (300 MPa), $\mu_e \approx 585$ remained constant from 1 kHz to 10 MHz, delivering exceptional frequency stability and flattened hysteresis behavior. These results establish stress-induced K_u as a central parameter for tailoring high-frequency magnetic performance and provide practical guidance for the design of soft magnetic materials. Such tunability addresses critical performance demands in advanced power electronics, including precision current transformers, EMC filters, and MHz-class switching devices for electric vehicles and 5G communication systems.

Received 8 September 2025; accepted 5 December 2025; published online 6 February 2026

1 Li J, Konstantinou G, Wickramasinghe HR, *et al.* Operation and control methods of modular multilevel converters in unbalanced AC grids: a review. IEEE J Emerg Sel Top Power Electron, 2019, 7: 1258–1271
2 Zhai L, Hu G, Lv M, *et al.* Comparison of two design methods of EMI filter for high voltage power supply in DC-DC converter of electric vehicle. IEEE Access, 2020, 8: 66564–66577
3 Kotb R, Chakraborty S, Tran DD, *et al.* Power electronics converters for electric vehicle auxiliaries: state of the art and future trends. Energies, 2023, 16: 1753
4 Fan Y, Guo Z, Wang M, *et al.* Phosphating-enhanced Fe-based amorphous soft magnetic composites with ultra-low power loss for efficient electrical energy conversion. Sci China-Phys Mech Astron, 2025, 68: 106112
5 Guo Z, Zheng X, Jin C, *et al.* A new Fe-based nanocrystalline soft magnetic composites with ultra-low core loss and superior DC-bias permeability up to megahertz-frequency. Mater Today Nano, 2025, 30: 100621
6 Périgo EA, Weidenfeller B, Kollár P, *et al.* Past, present, and future of soft magnetic composites. Appl Phys Rev, 2018, 5: 031301
7 Li FC, Liu T, Zhang JY, *et al.* Amorphous-nanocrystalline alloys: fabrication, properties, and applications. Mater Today Adv, 2019, 4: 100027
8 He J, Yuan H, Nie M, *et al.* Soft magnetic materials for power inductors: state of art and future development. Mater Today Electron, 2023, 6: 100066
9 Wu X, Li D, Li Z, *et al.* Amorphous FeNiCoCuSiBCr alloys with superior direct current tolerant characteristics. J Iron Steel Res Int, 2015, 22: 145–149
10 Yoshizawa Y, Yamauchi K. Effects of magnetic field annealing on magnetic properties in ultrafine crystalline Fe-Cu-Nb-Si-B alloys. IEEE Trans Magn, 1989, 25: 3324–3326
11 Petzold J. Applications of nanocrystalline softmagnetic materials for modern electronic devices. Scripta Mater, 2003, 48: 895–901
12 Herzer G. Modern soft magnets: Amorphous and nanocrystalline materials. Acta Mater, 2013, 61: 718–734
13 Willard MA, Daniil M. Chapter Four–Nanocrystalline Soft Magnetic Alloys Two Decades of Progress. In: Handbook of Magnetic Materials, Elsevier: Amsterdam. 2013, pp. 173–342.
14 Jiang M, Wang J, Cai M, *et al.* Improvement of soft magnetic properties for Fe-based amorphous/nanocrystalline alloy by longitudinal magnetic field annealing. J Non-Crystalline Solids, 2025, 650: 123382
15 Stoica M, Kolesar V, Bednarčic J, *et al.* Thermal stability and magnetic properties of partially Co-substituted $(Fe_{71.2}B_{24}Y_{4.8})_{96}Nb_4$ bulk metallic glasses. J Appl Phys, 2011, 109: 054901
16 Zhang Y, Sharma P, Makino A. Effects of cobalt addition in nanocrystalline $Fe_{83.3}Si_4B_8P_4Cu_{0.7}$ soft magnetic alloy. IEEE Transactions on Magnetics, 2014, 50: 1–4
17 Xu K, Ling H, Li Q, *et al.* Effects of Co substitution for Fe on the glass forming ability and properties of $Fe_{80}P_{13}C_7$ bulk metallic glasses. Intermetallics, 2014, 51: 53–58
18 Xue L, Yang W, Liu H, *et al.* Effect of Co addition on the magnetic properties and microstructure of FeNbBCu nanocrystalline alloys. J Magn Magn Mater, 2016, 419: 198–201
19 Liu T, Kong F, Xie L, *et al.* Fe(Co)SiBPCCu nanocrystalline alloys with high B s above 1.83 T. J Magn Magn Mater, 2017, 441: 174–179
20 Fan Y, Zhang S, Miao J, *et al.* Extremely high $B(Fe_{1-x}Co_x)_{86}Ni_1B_{13}$ amorphous soft magnetic alloys with good bending ductility. Intermetallics, 2020, 127: 106959
21 Hawelek L, Warski T, Wlodarczyk P, *et al.* Effect of Co substitution on crystallization and magnetic behavior of $Fe_{85.45-x}Co_xCu_{0.55}B_{14}$ metallic glass. Materials, 2020, 13: 919
22 Suetsuna T, Kinouchi H, Sanada N. Roles of cobalt and boron in FeCoBSi soft magnetic composite with in-plane uniaxial magnetic anisotropy. J Magn Magn Mater, 2021, 519: 167475
23 Cai M, Guo Z, Li L, *et al.* Obtaining extremely low coercivity of high B_s FeCoBSiCPCu nanocrystalline alloys through modulation of magnetic anisotropy. J Mater Sci Tech, 2025, 207: 105–112
24 Xiao M, Zheng Z, Ji L, *et al.* The role of V and Mo on crystallization process and magnetic properties of FeSiBCuNb alloys using in wide frequency scale. J Non-Crystalline Solids, 2019, 521: 119546
25 Wang Y, Xu J, Liu Y, *et al.* Microstructure evolution, magnetic properties and frequency characteristics of Si-rich FeSiBCuNb soft magnetic alloy induced by annealing treatment. Mater Charact, 2022, 187: 111830
26 Kraus L, Závěta K, Heczko O, *et al.* Magnetic anisotropy in as-quenched and stress-annealed amorphous and nanocrystalline $Fe_{73.5}Cu_1Nb_3Si_{13.5}B_9$ alloys. J Magn Magn Mater, 1992, 112: 275–277
27 Herzer G. Creep induced magnetic anisotropy in nanocrystalline Fe-Cu-Nb-Si-B alloys. IEEE Trans Magn, 1994, 30: 4800–4802
28 Hofmann B, Kronmüller H. Stress-induced magnetic anisotropy in nanocrystalline FeCuNbSiB alloy. J Magn Magn Mater, 1996, 152: 91–98
29 Cai M, Wang J, Wang Q, *et al.* Improvement of soft-magnetic properties for Fe-based amorphous alloys with high saturation polarization by stress annealing. Mater Res Lett, 2023, 11: 595–603
30 Cai P, He A, Zhang N, *et al.* Correlation between stress relaxation induced anisotropy, magnetic domain, and permeability of Co-doped FeCuSiBNbMn alloys. J Magn Magn Mater, 2023, 588: 171407

31 Guo Z, Yang X, Cai M, *et al*. Modulation of magnetic anisotropy and high-frequency soft-magnetic property of FeSiBNbCu nanocrystalline alloy via continuous tension annealing. Sci Sin-Phys Mech Astron, 2025, 55: 286118
32 Herzer G. Grain size dependence of coercivity and permeability in nanocrystalline ferromagnets. IEEE Trans Magn, 1990, 26: 1397–1402
33 Herzer G, Budinsky V, Polak C. Magnetic properties of FeCuNbSiB nanocrystallized by flash annealing under high tensile stress. Physica Status Solidi (b), 2011, 248: 2382–2388
34 Nutor RK, Fan X, He X, *et al*. Formation mechanism of stress-induced anisotropy in stress-annealed Fe-based nanocrystalline ribbon alloys. J Alloys Compd, 2019, 774: 1243–1249
35 Ohnuma M, Herzer G, Kozikowski P, *et al*. Structural anisotropy of amorphous alloys with creep-induced magnetic anisotropy. Acta Mater, 2012, 60: 1278–1286
36 He J, Huang Z, Xu J, *et al*. Microstructure evolution, stress state and electromagnetic performance of Fe-based nanocrystalline alloy induced by stress-annealing. J Mater Res Tech, 2024, 31: 447–457
37 Flohrer S, Schäfer R, Polak C, *et al*. Interplay of uniform and random anisotropy in nanocrystalline soft magnetic alloys. Acta Mater, 2005, 53: 2937–2942
38 Zhu F, Zhang J, Demidenko O, *et al*. Influence of stress-induced anisotropy on domain structure and magnetic properties of Fe-based nanocrystalline alloy under continuous tension annealing. J Non-Crystalline Solids, 2023, 600: 122035
39 Kurniawan I, Ito K, Seki T, *et al*. Microscopic correlation between magnetostriction and magnetic damping. Phys Rev B, 2025, 112: L100407
40 Yang F, Cai P, He A, *et al*. Effect of stress annealing on permeability and magnetic domains of FeCuSiBNbMn(Mo) amorphous alloys. J Mater Sci-Mater Electron, 2024, 35: 1111
41 Parsons R, Onodera K, Kishimoto H, *et al*. Effect of tensile stress during ultra-rapid annealing on the soft magnetic properties of Fe-B based nanocrystalline alloys. J Alloys Compd, 2022, 924: 166374
42 Peng K, Hu A, Wang D, *et al*. Influence of hydrogen on the magnetic properties of $Fe_{85}Zr_{3.5}Nb_{3.5}B_7Cu_1$ nanocrystalline alloy. Mater Chem Phys, 2005, 91: 289–292
43 Nosenko A, Mika T, Rudenko O, *et al*. Soft magnetic properties of nanocrystalline $Fe_{73}B_7Si_{16}Nb_3Cu_1$ alloy after rapid heating under tensile stress. Nanoscale Res Lett, 2015, 10: 136
44 Yang F, Zhang B, Man S, *et al*. Enhanced thermal-operating stability of high-frequency magnetic behavior for FeMnSiBNbCu nano-structural cores via field-annealing. Vacuum, 2021, 188: 110214
45 Sun Y, Li J, He A, *et al*. Influence of microstructure and anisotropy on the high-frequency soft magnetic properties of nanocrystalline FeSiBNbCuP alloys. J Magn Magn Mater, 2022, 560: 169639
46 Zhang R, He A, Xie L, *et al*. Correlation between dynamic magnetization process and dynamic domains of high saturation induction FeSiBNbCuMo nanocrystalline alloy with dual anisotropies. J Alloys Compd, 2022, 891: 161956
47 Sun H, Huan H, Wang C, *et al*. Magnetic properties, anisotropy, and domain structure of Fe-based nanocrystalline alloy induced by continuous stress-annealing treatment. J Magn Magn Mater, 2023, 569: 170430
48 Xu J. Structures and properties of nanocrystalline alloy with tension-induced anisotropy control. J Mater Sci-Mater Electron, 2023, 34: 370
49 Zhang R, He A, Cai P, *et al*. Nanostructural evolution and improved magnetic performance of high saturation-induction Fe-based alloy via two-step combination crystallization. Mater Charact, 2023, 205: 113317
50 Guo S, Li Y, Zhang Y, *et al*. Reduction of high-frequency core loss of a $Fe_{77.2}Si_{11}B_{8.5}Cu_{0.8}Nb_{2.5}$ soft magnetic nanocrystalline alloy by minor alloying. Acta Metall Sin (Engl Lett), 2024, 37: 1984–1992
51 Li XS, Su FC, Zhou J, *et al*. Ductile Fe-based amorphous alloy with excellent soft magnetic properties induced by low-temperature stress annealing. Intermetallics, 2024, 166: 108201
52 Chen Z, Wang J, Chen X, *et al*. High B_s nanocrystalline alloy with excellent soft magnetic properties achieved based on regulating amorphous matrix structure via two-step annealing. Intermetallics, 2025, 183: 108813
53 Flohrer S, Herzer G. Random and uniform anisotropy in soft magnetic nanocrystalline alloys (invited). J Magn Magn Mater, 2010, 322: 1511–1514
54 Kuhnt M, Marsilius M, Strache T, *et al*. Magnetostriction of nanocrystalline (Fe,Co)-Si-B-P-Cu alloys. Scripta Mater, 2017, 130: 46–48
55 Günes T. Novel method for construction of high performance nanocrystalline FeCuNbSiB toroidal core. J Alloys Compd, 2019, 804: 494–502
56 Saito K, Park HS, Shindo D, *et al*. Magnetic domain structure in $Fe_{78.8-x}Co_xCu_{0.6}Nb_{2.6}Si_9B_9$ nanocrystalline alloys studied by Lorentz microscopy. J Magn Magn Mater, 2006, 305: 304–309
57 Kwesi Nutor R, Xu X, Fan X, *et al*. Effects of applying tensile stress during annealing on the GMI and induced anisotropy of Fe-Cu-Nb-Si-B alloys. J Magn Magn Mater, 2019, 471: 544–548
58 Parsons R, Garitaonandia JS, Yanai T, *et al*. Effect of Si on the field-induced anisotropy in Fe-rich nanocrystalline soft magnetic alloys. J Alloys Compd, 2017, 695: 3156–3162
59 Kittel C. Physical theory of ferromagnetic domains. Rev Mod Phys, 1949, 21: 541–583

Acknowledgement This work was supported by the National Key R&D Program of China (2022YFB3804100), the National Natural Science Foundation of China (52231005), the Natural Science Foundation of Jiangsu Province (BK20221474), the Laboratory of Advanced Metallic Materials, Southeast University (AMM2025A01, AMM2024A02, and AMM2023B05), and the Science Technology Development Program of Yixing (C2024002). The authors thank the Center for Fundamental and Interdisciplinary Sciences of Southeast University for the support in magnetic domain measurement.

Author contributions Guo Z and Zhou J designed the research project; Guo Z, Zhou J and Liu Q fabricated the samples and performed the experiments and tests and wrote the draft of the manuscript; Cai M and Fan Y performed the magnetic tests; Guo Z and Luo Q conceptualized and supervised the research; Shen B and Guo Z contributed to the general discussion, conception, revision of the manuscript, and funding acquisition. All authors approved the version of the manuscript.

Conflict of interest The authors declare that they have no conflict of interest.

Supplementary information Supplementary materials are available in the online version of the paper.

Zhijun Guo received her PhD degree from Sichuan University during 2013–2019. She was under the Chinese Scholarship Council funded joint PhD at Queens University Belfast, UK during 2016–2018. She was a lecturer at China University of Mining and Technology during 2019–2022. She is currently an Associate Professor at Southeast University. Her research interests include dynamics, processing, properties and applications for soft magnetic materials and biomedical materials.

Jifeng Zhou is currently a PhD student in materials science and engineering at Southeast University. Her research interest focuses on the high-frequency loss mechanisms in iron-based nanocrystalline alloys for applications in third-generation semiconductor devices.

Qiang Luo received his PhD degree in condensed matter physics from the Institute of Physics, Chinese Academy of Sciences, in 2008, and was a postdoctoral researcher as a Humboldt scholar at the Leibniz Institute for Solid State and Materials Research, Dresden, Germany, during 2009–2011. He conducted research at Tongji University from 2012 to 2017. He is currently a professor at Southeast University. His research interests focus on the structures, dynamics, properties, and applications of amorphous and nanocrystalline alloys.

Baolong Shen received his PhD degree in engineering from Himeji Institute of Technology in 1999 and was a postdoctoral researcher then an assistant professor (faculty member) at the Institute for Materials Research, Tohoku University, Japan, during 1999–2007. He conducted research at Ningbo Institute of Materials Technology and Engineering, Chinese Academy of Sciences, from 2007 to 2012. He is currently the Chair Professor at Southeast University. His research interests focus on the formation, structures, properties, and applications of ferromagnetic disordered alloys.

应力调控各向异性实现铁基纳米晶合金MHz频段下稳定磁导率

郭志君[†], 周继凤[†], 刘茜茜, 蔡名娟, 凡艳舟, 罗强[*], 沈宝龙[*]

摘要 拉应力退火是一种有效调控软磁合金磁各向异性及高频性能的方法. 本文系统研究了拉应力退火对$Fe_{69.5}Co_3Nb_2Mo_{1.5}Si_{14}B_9Cu_1$纳米晶合金微观结构演化、磁畴演变及磁导率宽频稳定性的影响. 研究结果表明, 在0–300 MPa应力下, 感生磁各向异性常数(K_u)由22.5 J/m^{3}显著提升至665 J/m^3. 随着K_u的增强, 磁畴结构由不规则弯曲形状逐渐转变为均匀平直条带状, 平均磁畴宽度由110 μm减小至36 μm, 磁化机制由畴壁位移主导逐步转变为磁矩转动主导. 定量分析表明, 应力诱导各向异性虽导致低频磁导率(μ_e)下降, 但显著提升其高频稳定性. 当应力为50 MPa时, μ_e在1 MHz下为2330; 当应力为300 MPa时, μ_e在1 kHz至10 MHz宽频域内稳定保持在585, 表现出卓越的频率稳定性. 研究揭示, 应力诱导磁各向异性调控K_u与磁畴结构, 是实现MHz级磁导率稳定性的关键手段. 本工作为制备新一代高频软磁材料提供了理论指导与实验方法, 未来有望应用于精密电流互感器、EMC滤波器及MHz级电力电子器件的设计与生产.